applied sciences

MDPI

Article

Multi-Objective Optimization of Steel-Reinforced Concrete Hybrid Segment Support for TBM Tunnels Based on Surrogate Model

Guofang Yang [1], Dongming Liu [1], Qiang Guo [1], Guanfei Yang [1], Kun Li [2] and Bin Wang [2,*]

[1] CCCC-SHB Fourth Engineering Co., Ltd., Luoyang 471013, China; yangguofang163@163.com (G.Y.); liudongming2163@163.com (D.L.); guoqiang3163@163.com (Q.G.); yangguanfei4163@163.com (G.Y.)
[2] School of Civil & Architecture Engineering, Xi'an Technological University, Xi'an 710021, China; alexmoah113@outlook.com
* Correspondence: wangbin2346@xatu.edu.cn; Tel.: +86-135-1912-1853

Abstract

TBM tunnels crossing fault fracture zones require support systems for the control of deformation; ideally, these systems should be economically and computationally feasible to design. Conventional numerical optimization involves repeatedly evaluating high-fidelity models, and the associated computational burden increases rapidly as structural variables and competing objectives are introduced. This study develops and applies a surrogate-assisted multi-objective optimization framework for a steel-reinforced concrete hybrid segment support system in a tunnel located in a fault fracture zone. The framework combines Optimal Latin Hypercube Sampling (OLHS) for design-space coverage, Kriging surrogate modeling for rapid response prediction, SHapley Additive exPlanations (SHAP) for parameter importance interpretation, and the Non-dominated Sorting Genetic Algorithm II (NSGA-II) to conduct a Pareto search. Two engineering objectives—tunnel crown displacement and haunch displacement—are predicted using the surrogate model, while a material-based support cost index is evaluated independently from the design variables. The selected compromise solution reported in the original analysis reduces the crown displacement, haunch displacement, and support cost index by 7.02%, 9.28%, and 12.84%, respectively, relative to the reported original scheme. Direct numerical analysis of the selected continuous optimum yields crown and haunch displacements of approximately 2.25 and 1.27 mm, respectively, consistent with the surrogate-based results. Although available field monitoring observations provide an additional engineering consistency check, the short monitoring duration and incomplete documentation of the underlying project data limit claims of full-scale causal validation. The main contribution of this study is therefore the integration of expensive numerical analysis, interpretable surrogate modeling, multi-objective optimization, and engineering-level verification for the investigated hybrid segment system.

Keywords: multi-objective optimization; surrogate model; Kriging; OLHS; tunnel support; fault fracture zone; SHAP

Check for updates

Academic Editor: Weichung Yeih

Received: 18 September 2026
Revised: 22 October 2026
Accepted: 23 October 2026
Published: 24 October 2026

Copyright: © 2026 by the authors. Licensee MDPI, Basel, Switzerland. This article is an open access article distributed under the terms and conditions of the Creative Commons Attribution (CC BY) license.

1. Introduction

With the continued implementation of China's Western Development Strategy and the Belt and Road Initiative, infrastructure construction in western China has expanded rapidly. Tunnel boring machines (TBMs) are increasingly being used for large tunnel projects in central and western China due to their high excavation efficiency and operational safety [1].

Fault fracture zones are common adverse geological features in the mountainous areas of western China. Their poor stability, highly fractured rock, and low self-supporting capacity increase the risks of collapse, water inrush, and TBM jamming during excavation [2]. Accordingly, safe and effective support measures must be implemented in a timely manner to ensure that a TBM can reliably advance through such zones.

In recent years, extensive research has been conducted on tunnel support optimization. Li et al. [3] used the Yangshan Tunnel as a case study and combined multi-objective particle swarm optimization with FLAC^{3D} to minimize tunnel displacement. Qu et al. [4] performed tunnel support optimization based on the instability and deformation of red-bed surrounding rock during excavation. Cui et al. [5] developed a coupled inversion–optimization model for soft-rock tunnels, using back-analysis of rock properties to reduce support displacement. Yu et al. [6] developed a coordinated bolt–rock deformation model and optimized the bolt length and spacing via inverse analysis. Zhang et al. [7] combined reliability, robustness, and cost in Pareto-based design of shotcrete thickness and installation position. Liravi et al. [8] coupled a Latin-hypercube-trained surrogate with Bayesian optimization for tunnel geometry and material selection under dynamic soil–structure interactions. Structural studies provide complementary evidence for the selection of support configurations. Zhang et al. [9] validated a steel–concrete strengthening model against full-scale segment tests and identified that interface connectors govern load transfer. Ramesh et al. [10] modeled the Tabriz subway tunnels and showed how segment joints accommodate dip-slip fault movement. Research on concrete-filled steel pipe segments, layered steel–fiber concrete, and hybrid fiber–rebar reinforcement has identified the reinforcement layout and post-cracking stiffness as key design considerations, alongside load capacity [11–14]. Studies on interface failure and GFRP-reinforced alternatives have further emphasized the importance of load transfer and material selection [15,16]. Fault-crossing lining and ring-scale studies have linked damage to localized deformation, joint accommodation, and segment dimensions [17–21], and individual performance measures were improved when combining numerical models with optimization algorithms.

However, when using an optimization-based approach, the number of model evaluations increases rapidly with the number of design variables and objectives, consequently increasing computational cost and reducing efficiency. To address this issue, surrogate models have been introduced in engineering optimization research; as these models require relatively few samples and are inexpensive to evaluate, they can replace computationally expensive numerical models in tunnel, bridge, and other engineering applications. Zhao et al. [22] combined physics-based simulation, LightGBM prediction, and a multi-objective search to optimize the support parameters for the Huzhu Beishan Tunnel. Deng et al. [23] integrated CatBoost, SHAP, and NSGA-III for tunnel support optimization while balancing deformation control and cost. Kim et al. [24] used Hong Kong subway data and machine learning models tuned via Bayesian optimization to predict tunneling-induced surface settlement. Related studies have estimated ground–structure deformations, lining utilization, and earth pressure [25–27]; furthermore, optimization and simulation-based tools have been used for support displacement prediction, as well as shield operation and alignment selection [28–31]. Translating these advances into hybrid-ring designs requires interpretable parameter–response relationships and verification of the selected configuration, consistent with the priorities identified in recent reviews [32,33]. SHAP-based tunneling studies have addressed the interpretation requirement by explaining model predictions [34]. Kriging applications include ground–structure deformation prediction [25] and displacement-based parameter inversion [29], but these studies do not evaluate multi-component hybrid support designs. Research integrating Kriging with response interpretation, deformation–cost

optimization, and direct design verification remains limited for such support systems, particularly in tunnels crossing fault fracture zones.

This study develops a surrogate-model-based multi-objective optimization method for tunnel support structures. An actual tunnel project was considered, in order to optimize an S-RC (Steel-Reinforced Concrete) hybrid segment support structure for TBM excavation through a fault fracture zone. Crown displacement, haunch displacement, and support cost were selected as the objectives. The method is intended to maintain the stability of the surrounding rock while reducing the computational time and support cost. Kriging modeling [35], OLHS [36], NSGA-II [37], and SHAP [38] are integrated, each with a particular methodological contribution. The contribution of this study to the field of engineering is the application and verification of the proposed workflow for an S-RC support system crossing a fault fracture zone using direct FLAC^{3D} calculations and field monitoring. Accordingly, this study has two objectives: (1) to construct and validate an efficient and interpretable surrogate-assisted framework for crown displacement, haunch displacement, and support cost minimization and (2) to determine whether the selected design can reduce deformation and cost relative to the original scheme under the project conditions. Direct numerical verification and field comparisons provide complementary evidence of the selected design's deformation performance under the investigated fault zone conditions.

2. Materials and Methods

Figure 1 shows the multi-objective optimization workflow for the tunnel support structure. First, an initial excavation support model is built in ABAQUS. The optimization objectives are then selected according to the design requirements and project conditions, and the input and output variables of the surrogate model are defined. OLHS is used to generate parameter combinations within the specified ranges, and each combination is evaluated with the numerical model. A Kriging surrogate model is constructed in Isight and validated by comparing its predictions with the numerical results, as well as comparing its performance metrics to those of other surrogate models. SHAP analysis is then performed to quantify the contribution of each input variable to the predicted responses. Next, the Kriging input–output relationships are combined with the dimensionless least-squares objective to construct the multi-objective functions. These functions are solved with NSGA-II to obtain the Pareto-optimal solution set and select the optimal support scheme. Finally, the optimal scheme is compared with the original scheme and field measurements to evaluate its safety and support cost.

2.1. Engineering Background and Support System

The proposed method was applied to the Moxunshan Tunnel in Xinjiang, China. The tunnel has a diameter of 8.5 m and was excavated with an open TBM. The TBM-driven section is 8206 m long, and most of the surrounding rock is classified as Grade IV. A 100 m section from chainage PD1K79 + 923 to PD1K80 + 23 was selected for analysis. This section contains an approximately 25 m fault fracture zone, which is the focus of the optimization, and which intersects the tunnel axis at a high angle of approximately 60–70°, and there is no groundwater in this section.

During TBM excavation through the fault fracture zone, a new steel-reinforced concrete (S-RC) hybrid segment system was used. The system consists of steel segments, steel-reinforced concrete segments, and steel–concrete invert segments. Adjacent segments are connected by staggered, interlocking serrated joints, as shown in Figure 2. Each segment is 40 cm thick. Q235 steel is used for the steel plates. The main and side stiffeners are made of I14 I-sections and [14 channels, respectively, and HPB300 reinforcing bars are used.

The invert fill concrete and mesh-reinforced shotcrete have strength grades C25 and C30, respectively.

To enable the installation of the S-RC hybrid segmental support system in the Moxunshan Tunnel, the open-type TBM underwent specific modifications, including the adaptation of the segment erector, the installation of dedicated lifting devices and hoisting equipment, and the enhancement of the auxiliary thrust system. These modifications enabled the TBM to transition from its original excavation mode to an auxiliary-thrust, segment-supported excavation mode.

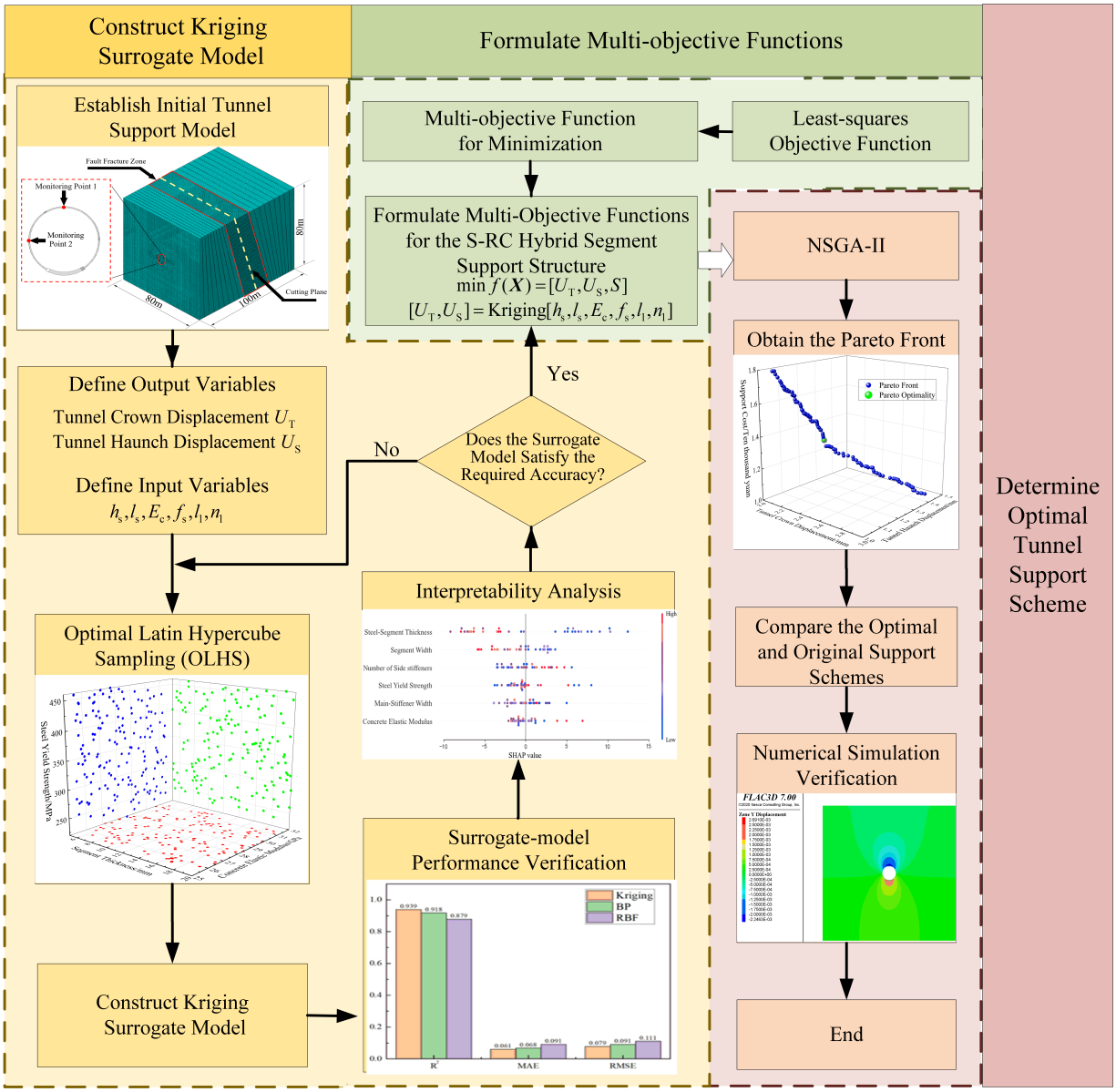


Figure 1. Multi-objective optimization workflow.

2.2. Numerical Modeling

The numerical model was first developed in ABAQUS (Ver. 2023) and subsequently imported into FLAC^{3D} (Ver. 7.0) for numerical analysis, all numerical modeling and simulations were performed on the same workstation equipped with an Intel Core Ultra 7 265K processor (3.90 GHz) and 64 GB of RAM. Specifically, the overall model of the surrounding rock mass, the excavation model, and the individual components of the tunnel support system were established separately in ABAQUS. The relevant components were organized

and categorized using the Set function to facilitate model identification and management. All components were then assembled into a unified finite element model, which was then exported in the ABAQUS input file format (*.inp) for subsequent import into FLAC^{3D} for further numerical analysis.

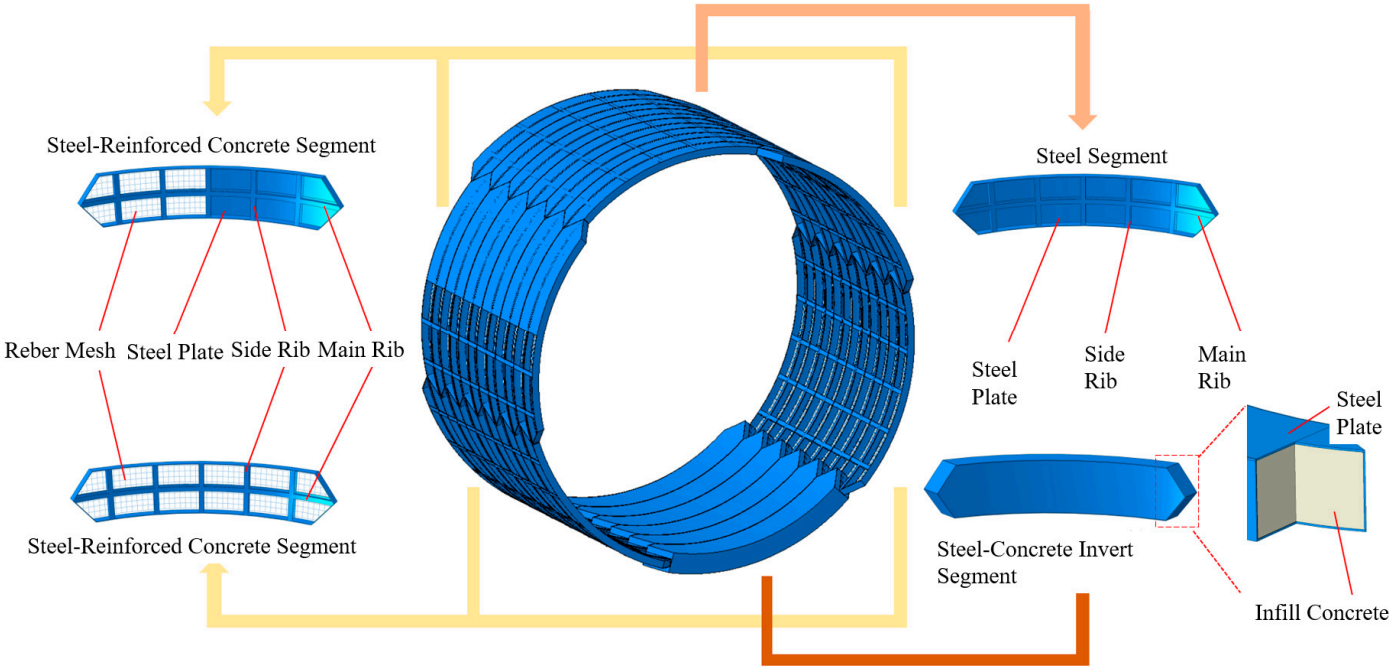


Figure 2. Schematic of the S-RC hybrid segment support structure.

The finite element model established in ABAQUS was configured as follows. According to Saint-Venant's principle, boundary effects must be considered when the distance from a lateral model boundary to the tunnel excavation contour is approximately 3–5 tunnel diameters. Therefore, both the model length and width were set to 80 m. With the modeled tunnel length included, the final model dimensions were 80 m × 80 m × 100 m. The model is shown in Figure 3. The fault fracture zone is outlined in red, the tunnel support structure is circled in red, and the section plane is shown by the yellow dashed line. Due to the complex geometry of the hybrid segment system—particularly the serrated joints and interfaces between different support components—a coarser mesh could not adequately represent the local geometric features and resulted in invalid or highly distorted elements. Therefore, the entire model consisted of 2,707,990 C3D8R elements with an element size of 1.5 m and 448,360 B31 elements with an element size of 0.01 m.

Throughout the whole calculation process, the individual serrated contacts between adjacent segments were not explicitly discretized. Instead, the segmented lining was idealized as an equivalent continuous structural system, with continuity imposed between adjacent segments. Consequently, local joint opening, frictional sliding, contact loss, and mechanical interlocking of the serrated surfaces were not directly reproduced.

In FLAC^{3D}, the Mohr–Coulomb elastoplastic model was used for the surrounding rock and concrete. This model was selected for its ability to describe the pressure-dependent shear strength of both materials in terms of cohesion and internal friction. The inclusion of a tension cutoff accounts for their limited tensile strength, enabling the model to represent both shear yielding and tensile failure.

As the version of FLAC^{3D} used in this study does not provide a dedicated von Mises plasticity model, the Drucker–Prager model was employed to represent the plastic behavior

of steel, with its parameters adjusted by setting the pressure-dependent parameter to zero so that the shear yield criterion reduced to the von Mises criterion.

Monitoring points 1 and 2 were selected in the model to match the field monitoring locations. The material properties of the surrounding rock and support structure are listed in Tables 1 and 2, respectively.

The calculation process in FLAC^{3D} was carried out as follows: First, the bottom boundary was fixed in all directions, the four lateral boundaries were constrained against displacement normal to their respective planes, and the top boundary was left free. Secondly, before tunnel excavation, gravitational loading was applied and the model was brought to equilibrium to establish the initial in situ stress state. Then, tunnel excavation and support installation were simulated incrementally using a nominal excavation advance of 3 m per step, which could be adjusted to represent the construction sequence, where necessary. Each construction cycle consisted sequentially of tunnel excavation, installation of the steel–concrete invert segment, installation of the first and second steel-reinforced concrete segments, installation of the steel segment, and advancement to the subsequent excavation step; this sequence was repeated to reproduce the progressive construction process and, during each cycle, the adopted stress-release mode was classified as a staged partial stress-release approach combining over-excavation-induced unloading with delayed support installation.

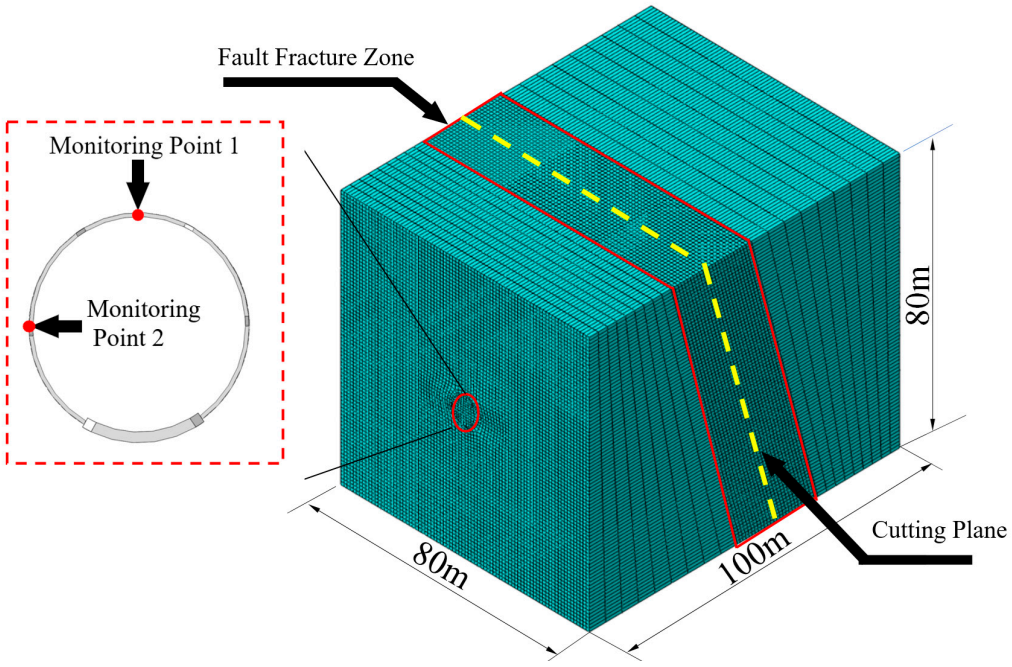


Figure 3. Numerical model.

Table 1. Material properties of the surrounding rock.

Surrounding	Density/ (kg/m^3)	Elastic Modulus/GPa	Poisson's Ratio	Cohesion/kPa	Internal Friction Angle/°
Grade IV	2630	3.15	0.30	1500	27
Fault fracture zone	2410	0.60	0.35	700	20

Table 2. Material properties of the support structure.

Component	Material	Unit Weight/(kN/m^3)	Elastic Modulus/GPa	Poisson's Ratio
Reinforcement mesh Steel plate	HPB300	78.5	200.00	0.30
Main stiffener Side stiffener	Q235	78.5	210.00	0.30
Shotcrete	C30	23.6	30.00	0.20
Infill concrete	C25	23.7	28.00	0.20

To verify the accuracy of the numerical model, the crown and haunch displacements predicted by FLAC^{3D} for the original support scheme were compared in Table 3 with the corresponding field actual monitoring data from the Moxunshan Tunnel.

Tunnel monitoring was performed using a JSS30A digital convergence meter (Shanghai Leiyun Testing Instrument Manufacturing Co., Ltd., Shanghai, China), with a measurement resolution of 0.01 mm and a nominal accuracy of 0.1 mm. To reduce random measurement errors and improve data reliability, repeated measurements were conducted at each monitoring point, and the arithmetic mean of the readings was adopted as the representative measured value.

Table 3. Comparison of numerical simulation results and field monitoring data.

Data Source	Crown Displacement/mm	Haunch Displacement/mm	Relative Error/%
FLAC^{3D}	2.42	1.40	11.68
Actual	2.74	1.49	6.04

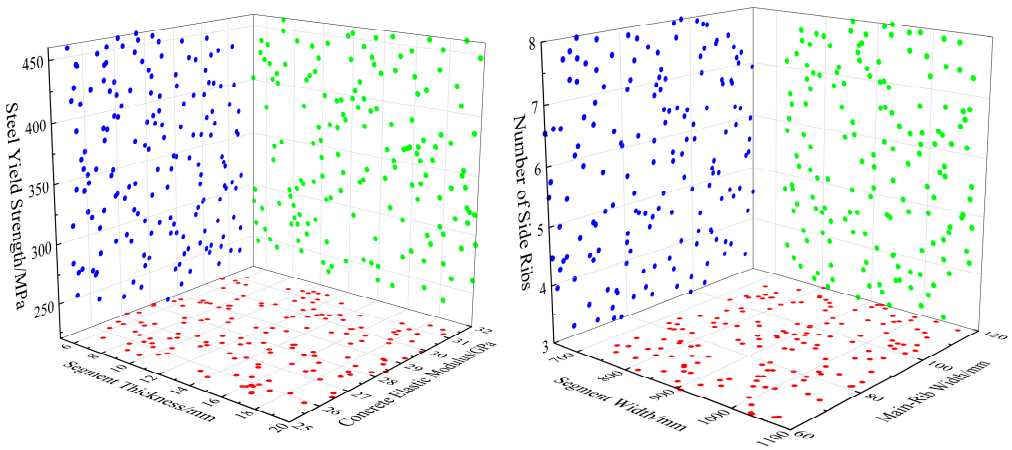
As shown in Table 3, the crown and haunch displacements from FLAC^{3D} were 2.42 mm and 1.40 mm, respectively, compared with the corresponding field measurements of 2.74 mm and 1.49 mm. The relative errors were 11.68% and 6.04%, respectively, indicating reasonable agreement between the numerical predictions and field observations and supporting the reliability of the numerical model.

2.3. Design Variables and Optimal Latin Hypercube Sampling

Based on relevant specifications [39,40] and the project conditions, the crown displacement U_T, haunch displacement U_S, and support cost S were selected as the optimization objectives. As the support cost S must be determined through comprehensive calculation based on the material parameters, geometric parameters, and other factors of the support structure, it was not directly adopted as an output parameter of the Kriging surrogate model. Therefore, only crown displacement U_T and haunch displacement U_S were selected as outputs of the Kriging surrogate model. Six input variables were considered; namely, steel segment thickness h_s, segment width l_s, shotcrete elastic modulus E_c, steel yield strength f_s, main stiffener width l_l, and number of side stiffeners n_l. All other parameters were kept constant. The ranges were defined, based on relevant specifications, construction safety requirements, and the available space [39–41], as follows: $h_s = [5, 20]$ mm, $l_s = [700, 1100]$ mm, $E_c = [25.5, 31.5]$ GPa, $f_s = [235, 460]$ MPa, $l_l = [60, 120]$ mm, and $n_l = [3, 8]$.

A sufficient sample size is required to balance the prediction accuracy of the Kriging model against the cost of numerical analysis. Optimal Latin hypercube sampling (OLHS) stratifies each input variable and optimizes sample placement to improve design-space coverage [36]. A total of 160 input combinations were generated within the specified ranges, and a numerical model was created for each combination. The models were analyzed in FLAC^{3D} to obtain the output responses. Figure 4 shows the sample distribution, while

Table 4 lists the selected input variables and provides the corresponding numerical results. As n_1 is discrete, its sampled value was rounded to an integer.



(**a**) $h_s - E_c - f_s$ (**b**) $l_s - l_1 - n_1$

Figure 4. OLHS projections of the input variables.

Table 4. Selected input variables and corresponding numerical results.

No.	h_s/mm	E_c/GPa	f_s/MPa	l_s/mm	l_l/mm	n_1	U_T/mm	U_S/mm
1	13.97	25.59	239.77	815.94	70.25	4	2.87	1.34
2	19.77	29.30	247.86	973.26	110.65	4	2.21	1.08
3	19.09	31.38	243.38	857.52	74.77	5	2.57	1.21
⋮	⋮	⋮	⋮	⋮	⋮	⋮	⋮	⋮
158	6.66	28.64	238.92	839.34	61.81	6	2.78	1.28
159	7.49	25.65	271.38	987.66	65.73	7	2.45	1.11
160	10.73	29.15	298.57	792.36	63.62	4	2.57	1.30

2.4. Kriging Surrogate Model

A surrogate model is an approximate function constructed from a limited number of design variable combinations and corresponding optimization results, which generally provides high-accuracy predictions at very low computational cost [35]. Compared with other surrogate approaches, the Kriging model performs unbiased optimal estimation based on regionalized variables and spatial variograms, offers strong nonlinear fitting capability and high approximation accuracy, and does not require an explicit mathematical model [35]. Therefore, a Kriging surrogate model was adopted in this study to solve the multi-objective optimization problem for the tunnel support structure.

2.4.1. Kriging Formulation

To approximate the multi-objective model with a Kriging model, the design variables must first be defined. The optimization parameter vector $\boldsymbol{X}$ and the multi-objective function vector $f(\boldsymbol{X})$ are used as the Kriging input and output, respectively. The resulting approximation can be expressed as

$$y(\boldsymbol{X}) = f(\boldsymbol{X})^{\mathrm{T}}\boldsymbol{\beta} + Z(\boldsymbol{X}) \quad (1)$$

where $y(\boldsymbol{X})$ is the response vector predicted by the Kriging model; $\boldsymbol{\beta} = [\beta_1, \beta_2 \cdots \beta_j]^{\mathrm{T}}$ is the least-squares estimate of the regression coefficient vector; and $Z(\boldsymbol{X})$ is a stationary random

process with zero mean and variance σ^2. For any two vectors $\boldsymbol{X}^p$ and $\boldsymbol{X}^q$ in the design variable domain, the covariance of $Z(\boldsymbol{X})$ is expressed as follows:

$$\mathrm{Cov}[Z(\boldsymbol{X}^p), Z(\boldsymbol{X}^q)] = \sigma^2 R(\boldsymbol{\theta}, \boldsymbol{X}^p, \boldsymbol{X}^q) \tag{2}$$

$$R(\boldsymbol{\theta}, \boldsymbol{X}^p, \boldsymbol{X}^q) = \exp\left[-\sum_{m=1}^{j} \theta_m (x_m^p - x_m^q)^2\right] \tag{3}$$

where $R(\boldsymbol{\theta}, \boldsymbol{X}^p, \boldsymbol{X}^q)$ is the correlation function between the vectors $\boldsymbol{X}^p$ and $\boldsymbol{X}^q$. The function varies inversely with the relative distance between the variables and is defined using a Gaussian function (Gauss), where p and q are sample point indices, $p, q = [1, 2 \ldots, n]$; $\boldsymbol{\theta}$ is the weight coefficient vector of the correlation function; θ_m is the m-th component of $\boldsymbol{\theta} = [\theta_1, \theta_2 \cdots \theta_i]$; and x_m^p and x_m^q are the m-th components of $\boldsymbol{X}^p$ and $\boldsymbol{X}^q$, respectively.

Based on maximum likelihood estimation, the correlation parameter $\boldsymbol{\theta}$ in Equations (2) and (3) can be obtained as follows:

$$\boldsymbol{\theta}^* = \mathrm{argmax}\left[-\frac{1}{2}\ln|\boldsymbol{R}(\boldsymbol{\theta})| - \frac{1}{2}\ln\hat{\sigma}^2(\boldsymbol{\theta})\right] \tag{4}$$

$$\begin{cases} \hat{\sigma}^2 = \frac{1}{n}(\boldsymbol{G} - \boldsymbol{F}\hat{\boldsymbol{\beta}})^{\mathrm{T}} \boldsymbol{R}^{-1}(\boldsymbol{G} - \boldsymbol{F}\hat{\boldsymbol{\beta}}) \\ \hat{\boldsymbol{\beta}} = (\boldsymbol{F}^{\mathrm{T}}\boldsymbol{R}^{-1}\boldsymbol{F})^{-1}\boldsymbol{F}^{\mathrm{T}}\boldsymbol{R}^{-1}\boldsymbol{G} \end{cases} \tag{5}$$

where $\boldsymbol{\theta}^*$ is the maximum likelihood estimate of $\boldsymbol{\theta}$; $\boldsymbol{R}$ is the correlation matrix $R(\boldsymbol{X}^p, \boldsymbol{X}^q)$ for the sample points; $\hat{\sigma}^2$ is the estimated process variance; $\hat{\boldsymbol{\beta}}$ is the maximum likelihood estimate of $\boldsymbol{\beta}$; $\boldsymbol{G}$ is the vector of objective values obtained from the available data; and $F = [1, 1 \ldots, 1]^{\mathrm{T}}$

Combining Equations (1)–(5), an optimization algorithm is used to find the value of θ that maximizes the likelihood function, thereby effectively ensuring the accuracy of the constructed model.

In summary, the Kriging model provides the prediction $\hat{y}(x)$ corresponding to the optimization variables $\boldsymbol{X}$ for the multi-objective function $f(\boldsymbol{X})$. The prediction is expressed as follows:

$$\hat{y}(x) = \boldsymbol{F}(\boldsymbol{X})^{\mathrm{T}}\hat{\boldsymbol{\beta}} + r(x)^{\mathrm{T}}\boldsymbol{R}^{-1}(\boldsymbol{G} - \boldsymbol{F}\boldsymbol{\beta}) \tag{6}$$

where $r(x) = \left[R(X, X^1), R(X, X^2) \ldots, R(X, X^q)\right]$.

The Kriging surrogate model is constructed by substituting the multi-objective functions into Equation (1) and solving Equations (1)–(6). The model can then be used to predict the objectives from the available samples and a new set of design variables.

2.4.2. Training and Validation Protocol

A Gaussian function was used as the basis function, and the DOE and Approximation modules in Isight were used to construct the Kriging surrogate model. The 160 input sets and corresponding numerical results were first treated as reference data and preprocessed. A total of 15 samples with abnormal numerical responses were excluded from training because either the simulated crown displacement exceeded 3.5 mm or the simulated haunch displacement exceeded 1.2 mm, the remaining data was divided into 80% for training and 20% for validation, while valid responses were retained to preserve coverage of the design space. Five-fold cross-validation was performed on the training set to assess the predictive performance of the Kriging surrogate model [25]. The trained model was then evaluated on the independent validation set by comparing its predictions with the corresponding numerical simulation results [28].

To assess predictive performance further, the following three metrics were used: the coefficient of determination (R^2), root mean square error (RMSE), and mean absolute error (MAE). R^2 is dimensionless, whereas RMSE and MAE are expressed in millimeters (mm).

On the 145 selected input sets, the Kriging model was compared with a backpropagation (BP) neural network model and a radial basis function (RBF) model based on the values of these metrics [30]. The expressions for the BP and RBF models are given as follows:

$$\hat{y}_{\mathrm{BP}} = W_2 f(W_1 x + b_1) + b_2 \tag{7}$$

$$\hat{y}_{\mathrm{RBF}}(x) = b + \sum_{j=1}^{m} w_j \exp\left(-\frac{\|x - c_j\|^2}{2\sigma_j^2}\right) \tag{8}$$

where x is the input feature vector, W_1 is the input-to-hidden weight matrix, W_2 is the hidden-to-output weight matrix, b_1 is the hidden-layer bias vector, b_2 is the output-layer bias vector, b is the output bias vector, σ_j is the width (spread) parameter, c_j is the center vector, and w_j is the output weight vector.

The BP networks for outputs A and B were configured with hidden-layer structures of (8, 4) and (8), respectively. The activation functions were tanh and ReLU, with L-BFGS optimization, regularization coefficients of 10 and 0.01, and a maximum of 650 iterations. For the RBF models, 16 and 12 K-means centers were used for A and B, respectively, with a Gaussian basis parameter $\gamma = 2.0$ and ridge regularization coefficients of 10^{-5} and 0.1. A random seed of 123 was used for both models to ensure reproducibility.

2.5. Multi-Objective Optimization

2.5.1. Objective Functions and Constraints

Establishing an objective function is a prerequisite for multi-objective optimization. Different objective functions respond differently to relative errors in test curves, which can affect both model convergence and the optimization results. The objectives may differ in units and magnitude. As direct optimization can bias the results toward objectives with larger numerical scales, the objectives were converted to dimensionless form to make them comparable [29]. The least-squares method is unbiased and has minimum-variance properties. For minimization problems, it gives each optimization parameter equal weight and is straightforward to solve. The dimensionless least-squares objective function is expressed as follows [42]:

$$f(x) = \sqrt{\frac{1}{N} \cdot \sum_{n}^{N} \left(\frac{M_n^{\mathrm{t}} - N_n^{\mathrm{t}}}{M_n^{\mathrm{t}}}\right)^2} \times 100\% \tag{9}$$

where x is the optimization parameter; $f(x)$ is the objective function; N is the number of monitoring points; M_n^{t} and N_n^{t} are the measured and simulated values at the n-th tunnel monitoring point, respectively.

Equation (9) provides a dimensionless root-mean-square relative error measure for evaluating the discrepancy between measured and simulated displacements at tunnel monitoring points. This formulation enables the prediction error of an individual response to be evaluated independently of its magnitude. However, tunnel support optimization involves multiple performance criteria which may exhibit competing relationships. Therefore, a single scalar error function cannot adequately represent the simultaneous optimization of these engineering objectives. To account for their individual contributions and potential trade-offs, the optimization problem is formulated as a vector of objective functions can be expressed as [32]

$$\begin{cases} \min F(\boldsymbol{X}) = [f_1(x), f_2(x), \cdots f_i(x)]^{\mathrm{T}} \\ \text{s.t. } \boldsymbol{X} = [x_1, x_2, \cdots x_j]^{\mathrm{T}} \\ \quad i \geq 2\,; j \geq 2 \end{cases} \tag{10}$$

where $\boldsymbol{X}$ is the optimization parameter vector; $F(\boldsymbol{X})$ is the multi-objective function vector; i and j are the numbers of optimization objectives and optimization parameters, respectively.

To improve stability while controlling support cost, the crown displacement U_T, haunch displacement U_S, and support cost S were selected as optimization objectives. The optimization parameters were $h_s, l_s, E_c, f_s, l_l, n_l$, and their prescribed input ranges were adopted as constraints. Based on Equation (10), the Kriging-based multi-objective functions and constraints were formulated as follows:

$$\min F(\boldsymbol{X}) = [U_T, U_S, S] \tag{11}$$

$$[U_T, U_S] = \text{Kriging}[h_s, l_s, E_c, f_s, l_l, n_l] \tag{12}$$

$$\begin{cases} 5\text{ mm} \le h_s \le 20\text{ mm} \\ 700\text{ mm} \le l_s \le 1100\text{ mm} \\ 60\text{ mm} \le l_l \le 120\text{ mm} \\ 25.5\text{ GPa} \le E_c \le 31.5\text{ GPa} \\ 235\text{ MPa} \le f_s \le 460\text{ MPa} \\ 3 \le n_l \le 8 \end{cases} \tag{13}$$

where $\min F(\boldsymbol{X})$ is the optimal support scheme oriented toward objective minimization; $[U_T, U_S, S]$ is the optimization objective output when the design parameter is $[h_s, l_s, E_c, f_s, l_l, n_l]$; and the support cost S is calculated as follows [43]:

$$S = (V_{c1}P_{c1} + V_{c2}P_{c2}) + \gamma_s V_s P_s + \gamma_r V_r P_r \tag{14}$$

where V_{c1}, V_{c2}, V_s, and V_r are the volumes of shotcrete, infill concrete, steel, and reinforcement, respectively; P_{c1}, P_{c2}, P_s, and P_r are the corresponding unit prices of shotcrete, infill concrete, steel, and reinforcement, respectively; γ_s and γ_r are the unit weights of the steel and reinforcement, respectively.

The material cost was estimated for a unit tunnel length of 1 m, based on the geometric dimensions of the support components and indicative material prices reflecting local market conditions in Xinjiang, China, for the third quarter of 2025. For the original support scheme, the estimated quantities of C30 shotcrete, C25 plain concrete, Q235 structural steel, and reinforcement were 2.20 m^3, 1.21 m^3, 3.3114 t/m, and 0.60 t/m, respectively. The corresponding reference unit prices were taken as RMB 300/m^3, 250/m^3, 3550/t, and 3360/t, respectively. A consistent pricing basis and calculation length were adopted for the original and optimized support schemes, with the cost assessment limited to the four constituent materials.

2.5.2. NSGA-II Configuration

NSGA-II is a multi-objective evolutionary algorithm based on non-dominated sorting, which is widely used for multi-objective optimization as its fast non-dominated sorting procedure reduces computational complexity and improves convergence [37].

The NSGA-II procedure is shown in Figure 5. An initial population is first generated and defined as the parent population, and the iteration counter I is set to 0. Fast non-dominated sorting and crowding distance calculation are then performed. Selection, crossover, and mutation operations are applied to generate the offspring population, the parent and offspring populations are merged, and non-dominated sorting and crowding distance calculation are repeated to form the next population. If I is less than I_{max}, selection, crossover, and mutation are repeated; otherwise, the process stops, and the Pareto-optimal solutions are output.

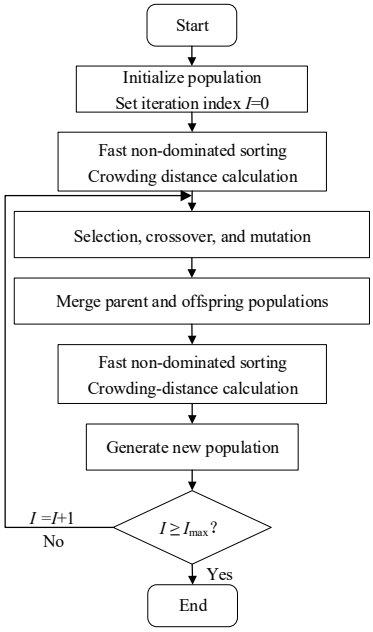


Figure 5. Flowchart of the NSGA-II algorithm.

The NSGA-II algorithm was implemented in Isight, with a population size of 160 and 1000 iterations, conventional multi-objective optimization would require 1.6×10^5 numerical analyses, which is impractical for a complex numerical model. In contrast, the Kriging surrogate model predicts the objectives at low computational cost and avoids most repeated analyses. The Kriging-based objective functions were coupled with NSGA-II in Isight. The population size was 160, the number of iterations was 1000, and the crossover probability was 0.8. The crossover and mutation distribution indices were set to 10.0 and 20.0, respectively, to control the distribution of offspring generated during the crossover and mutation operations, and the optimization variables were constrained within the prescribed ranges defined in Equation (13). As Isight supports the definition of parameters as integers and setting discrete allowable values, n_1 was output as an integer after NSGA-II calculation.

2.5.3. Pareto-Optimal Solution Selection

Pareto-optimal solutions are required for multi-objective optimization. A single-objective problem generally has one optimum, whereas a multi-objective problem may produce a set of solutions due to interactions between its design variables [37]. This set will contain solutions that are not dominated by any other solution, the projection of which into the objective space forms the Pareto front, marking the boundary of the feasible region. An example Pareto-optimal solution set is shown in Figure 6.

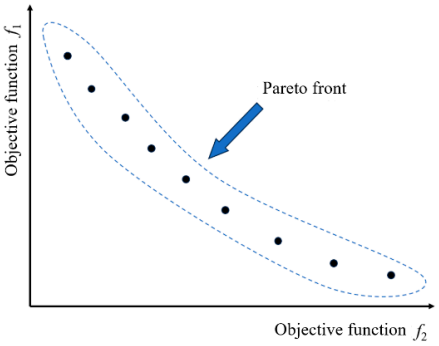


Figure 6. Schematic of a Pareto-optimal solution set.

As no single solution minimizes all three objectives, the Pareto solutions were evaluated using the ideal-point distance method [23]. Each objective was normalized, and the solution nearest to the ideal point formed from the individual minimum was selected.

To eliminate the influence of differences in units and numerical scales among the optimization objectives, the objective function values in the Pareto solution set were first normalized using the min–max normalization, which can be expressed as

$$f_k^{\text{norm}}(x) = \frac{f_k(x) - f_k^{\min}}{f_k^{\max} - f_k^{\min}} \tag{15}$$

where k is the number of the objective function, $k = [1, 2, 3]$, $f_k^{\text{norm}}(x)$ is the normalized value of the k-th objective function, $f_k(x)$ is the original value of the k-th objective function; $f_k^{\min}$, $f_k^{\max}$ are the minimum and maximum values of the k-th objective function within the obtained Pareto solution set, respectively; and x is the vector of design variables.

After normalization, the ideal point was defined as ($\boldsymbol{f}^* = (0, 0, 0)$). Equal weights were assigned to U_T, U_S, S, and support cost were considered equally important in the decision-making process. The weighted Euclidean distance between each Pareto solution and the ideal point was calculated as

$$D(x) = \sqrt{\sum_{k=1}^{3} w_k \left(f_k^{\text{norm}} - f_k^*\right)^2} \tag{16}$$

where $D(x)$ is the weighted Euclidean distance, w_k is weight, and $w_1 = w_2 = w_3 = \frac{1}{3}$. The Pareto solution with the minimum distance to the ideal point was selected as the final optimal compromise support scheme.

2.6. SHAP Analysis

Accurate surrogate models are not always easy to interpret. The SHAP (SHapley Additive exPlanations) value measures the contribution of an input variable to the predicted response, making predictions easier to interpret [38]. Accordingly, SHAP analysis was applied to the Kriging model. The model-agnostic KernelExplainer implemented in Python (Ver. 3.14) was used to calculate the SHAP values and interpret the predictions of the Kriging surrogate model. The KernelExplainer was implemented using the 145 retained valid samples as the background dataset.

The results are reported in the same analytical sequence as the above-mentioned procedures; namely, surrogate validation, SHAP-based feature interpretation, and optimization with numerical and field verification.

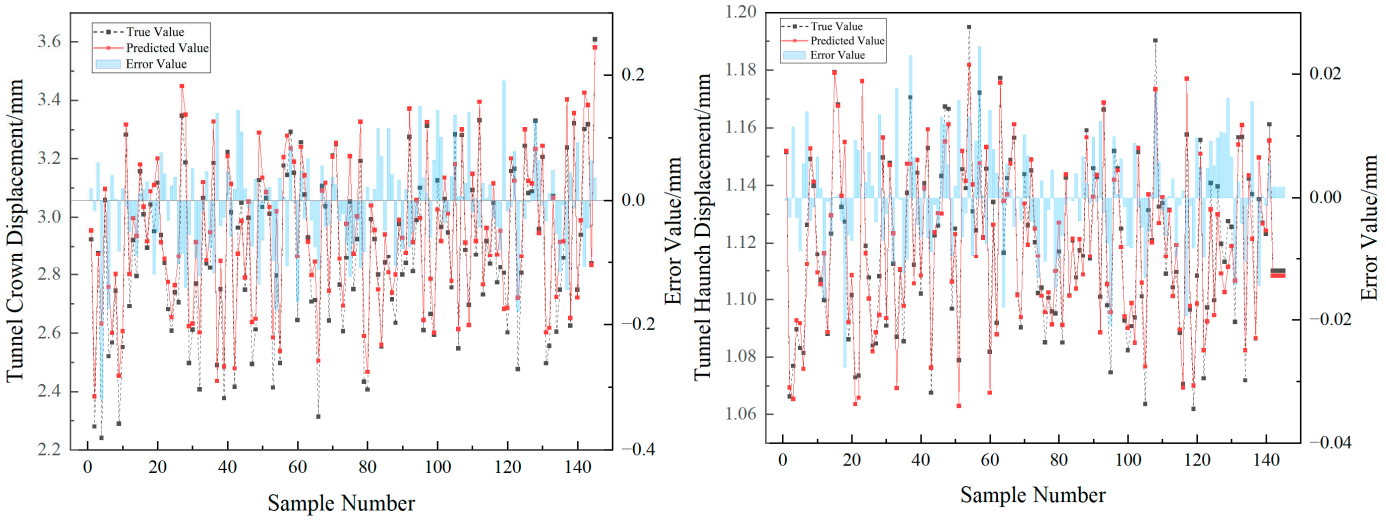
3. Results

3.1. Predictive Performance of Surrogate Model

As shown in Figure 7, the close agreement between the Kriging predictions and reference values for both outputs indicates that the model can accurately predict the displacements of the S-RC hybrid segment support structure.

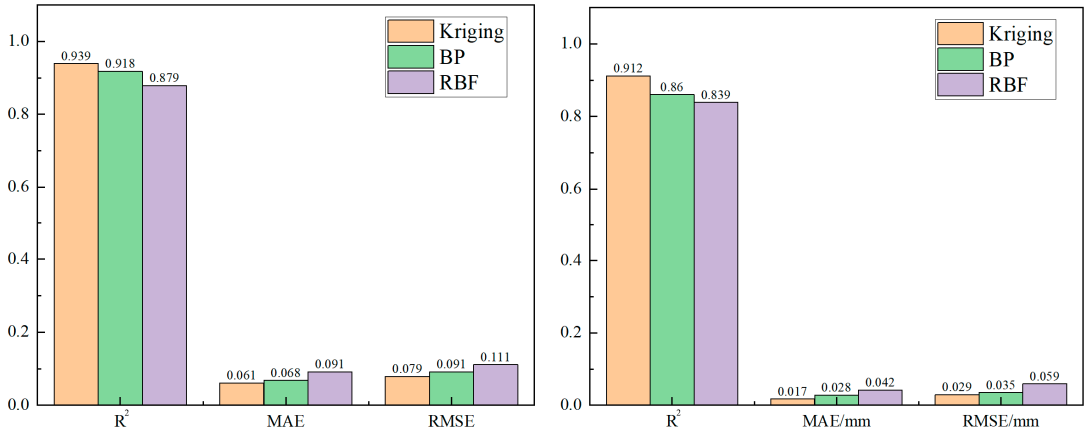
The evaluation results for the three surrogate models are presented in Figure 8, from which we see that the Kriging model exhibited superior predictive performance compared with the BP and RBF models. For crown displacement, the Kriging model achieved R^2 values that were 2.29% and 6.83% higher than those of the BP and RBF models, respectively, while its MAE values were 10.29% and 32.97% lower, and its RMSE values were 13.19% and 28.83% lower, respectively. Similarly, for haunch displacement, the R^2 values of the Kriging model were 6.05% and 8.70% higher, the MAE values were 39.29% and 59.52% lower, and the RMSE values were 17.14% and 50.85% lower than those of the BP and RBF

models, respectively. These results demonstrate that the Kriging model provides higher prediction accuracy and lower prediction errors than the BP and RBF models for both crown and haunch displacements. Therefore, the Kriging model was selected for subsequent multi-objective optimization.



(**a**) Tunnel crown displacement (**b**) Tunnel haunch displacement

Figure 7. Comparison of reference values and Kriging predictions.



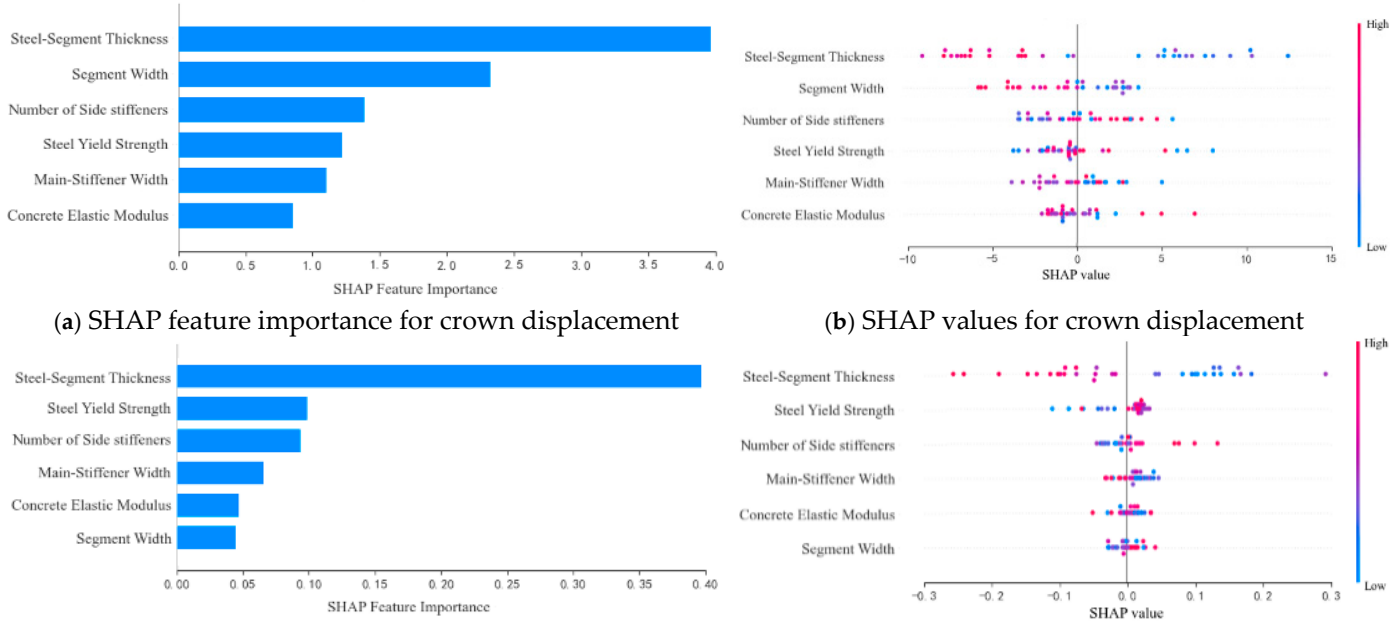
(**a**) Tunnel crown displacement (**b**) Tunnel haunch displacement

Figure 8. Comparison of evaluation metrics for different surrogate models.

3.2. SHAP Analysis

Figure 9 presents the SHAP results. Red points indicate high input values, while blue points indicate low values. All SHAP values were standardized using the Z-score method to facilitate consistent interpretation and comparison across different input variables. As the crown and haunch displacements were minimized, a negative SHAP value indicates that an input reduces the predicted displacement and therefore has a favorable effect, while a positive value indicates an unfavorable effect.

As shown in Figure 9a,b, the input variables for crown displacement were ranked as follows: steel segment thickness (3.91) > segment width (2.36) > number of side stiffeners (1.45) > steel yield strength (1.31) > main stiffener width (1.14) > concrete elastic modulus (0.82). This ranking demonstrates that crown displacement is most sensitive to the overall stiffness of the support structure.



(**a**) SHAP feature importance for crown displacement

(**b**) SHAP values for crown displacement

(**c**) SHAP feature importance for haunch displacement

(**d**) SHAP values for haunch displacement

Figure 9. SHAP analysis results.

As shown in Figure 9c,d, the input variables for haunch displacement were ranked as follows: steel segment thickness (0.39) > steel yield strength (0.11) > number of side stiffeners (0.09) > main stiffener width (0.07) > concrete elastic modulus (0.04) > segment width (0.03). This order differs from that for crown displacement, and the smaller SHAP magnitudes indicate that haunch displacement is less sensitive to the input variables. The SHAP values decrease as steel segment thickness and main stiffener width increase, but rise with the number of side stiffeners and steel yield strength. Thus, haunch displacement is also affected by support stiffness, albeit less strongly than crown displacement. The concrete elastic modulus and segment width show clearly nonlinear effects, and their ranges should be carefully considered together with the other parameters during optimization.

3.3. Multi-Objective Optimization and Verification

To evaluate the convergence performance of the NSGA-II algorithm and the stability of the obtained Pareto solution set, the Pareto fronts obtained after gen =300, 500, 800, and 1000 were compared in Figure 10.

As shown in Figure 10, when gen = 300, the non-dominated solutions exhibit a relatively scattered and irregular distribution, without a clearly defined Pareto front; when gen = 500, the non-dominated solutions gradually become more concentrated, and an overall distribution trend begins to emerge, although a certain degree of dispersion remains; when gen = 800, the overall shape of the Pareto front becomes more distinct, with the non-dominated solutions exhibiting a more organized distribution along the front, although some scattered solutions are still observed; when gen = 1000, he dispersion of the Pareto solutions decreases considerably, and the non-dominated solutions become a more clearly defined and continuous front.

Figure 10 shows that the distribution of the Pareto solutions progressively improves with increasing generations, and the Pareto front evolves from a scattered and irregular configuration toward a more concentrated and organized distribution. Although some dispersion persists, the relatively organized distribution of the solutions at 1000 generations suggests that the algorithm has achieved substantial Pareto Optimality convergence, providing a sufficiently developed set of Pareto for subsequent optimal scheme selection.

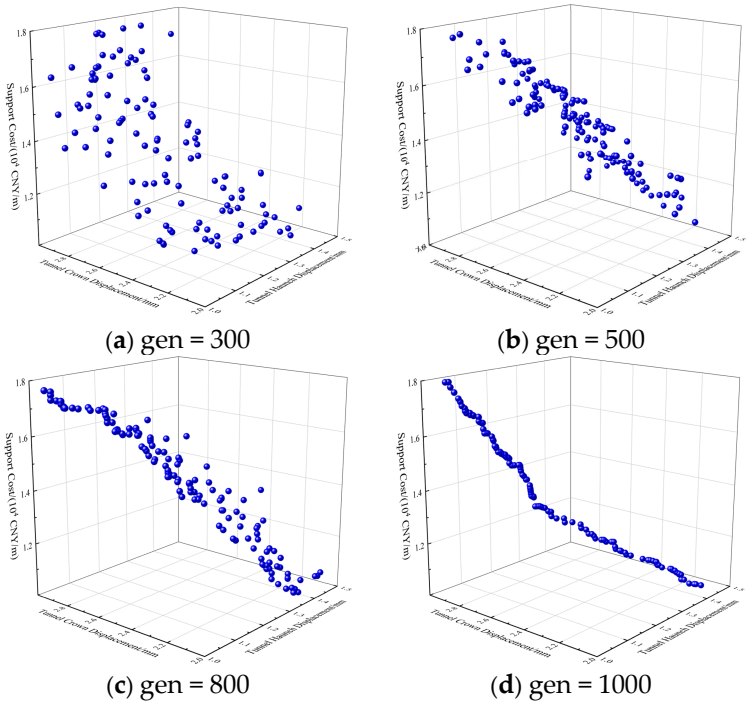


Figure 10. Pareto frontier in different iterative steps.

Figure 11 shows the resulting Pareto-optimal solution set, in which the blue points form the Pareto front and the green point is the selected optimal solution.

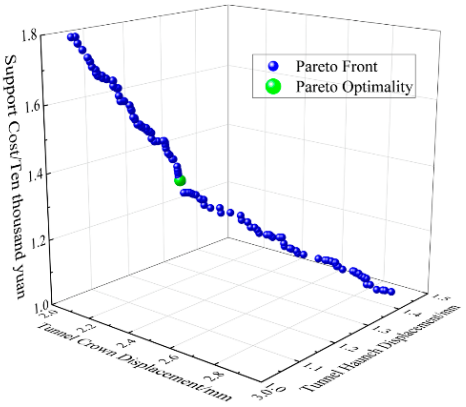


Figure 11. Pareto-optimal solution set.

The Pareto front shows a clear trade-off among the three objectives; in particular, improving one objective can worsen one or both of the others, and the objectives cannot all reach their individual minima at the same time. Consequently, the three objectives cannot simultaneously attain their individual theoretical optima and a Pareto-optimal solution must be selected to achieve the best overall compromise.

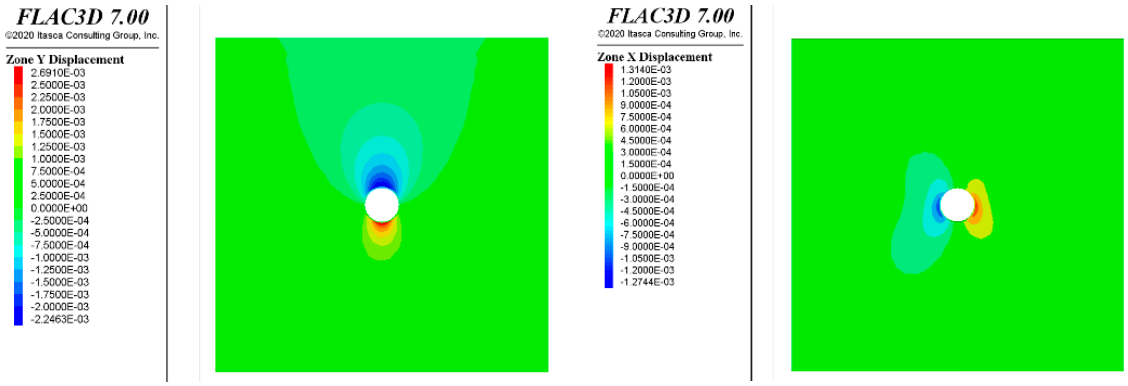
As shown in Figure 11, the optimal solution was combined with its corresponding design parameters to define the optimal support scheme, which was then compared with the original scheme. The optimization results are listed in Table 5. The crown displacement U_T, haunch displacement U_S, and support cost S were reduced by 7.02%, 9.28%, and 12.84%, respectively. Meanwhile, a single FLAC^{3D} numerical simulation required approximately 15 min, whereas the NSGA-II optimization using the trained Kriging surrogate models, with a population size of 160 and 1000 generations, was completed in approximately 7 min. The time cost shows the entire evolutionary optimization stage required only slightly

more computational time than a single FLAC^{3D} analysis. Thus, the Kriging-based method effectively reduced tunnel deformation and support cost while improving computational efficiency by minimizing the need for repeated numerical simulations.

Table 5. Comparison of the original and optimal support schemes.

Support Scheme	h_s/mm	E_c/GPa	f_s/MPa	l_s/mm	l_l/mm	n_1	U_T/mm	U_S/mm	$S/(10^4$CNY/m)
Original	10.00	30.00	235.00	900.00	80.00	5	2.42	1.40	1.48
Optimal	9.05	25.71	235.65	771.51	75.04	6	2.25	1.27	1.29

The parameters of the optimal support scheme were analyzed in FLAC^{3D} to verify the Kriging predictions, and the results are shown in Figure 12, and the unit of data shown in Figure 12 is m.



(**a**) Tunnel crown displacement (**b**) Tunnel haunch displacement

Figure 12. Numerical results for the optimal support scheme.

As shown in Figure 12, the FLAC^{3D} results for the optimal support scheme were 2.246 mm for crown displacement and 1.274 mm for haunch displacement. The errors relative to the Kriging predictions in Table 4 were approximately 0.18% and 0.31% for crown and haunch displacements, respectively. The close agreement confirms the accuracy of the Kriging predictions and the reliability of the proposed multi-objective optimization method.

To conform to standard material specifications and practical fabrication requirements, minor adjustments were made to the optimized parameters listed in Table 5 before their implementation in the Moxunshan Tunnel. Specifically, h_s, E_c, f_s, l_s, l_l were adjusted from 9.05 to 9 mm, 25.71 to 25.5 GPa, 235.65 to 235 MPa, 771.51 to 770 mm, 75.04 to 75 mm, respectively. Field monitoring was also conducted in tunnel sections supported with the original and optimal schemes. Two monitoring cross-sections within the fault fracture zone were selected for comparison, located approximately 2.5 m inside the entrance and 2.5 m before the exit of the fault zone, respectively. Both sections were located within the same geological zone and had comparable ground conditions. To assess the safety of the optimal scheme, the monitoring results are compared in Figure 12.

As shown in Figure 13, the measured crown and haunch displacements were lower with the optimal support scheme. The maximum measured values after optimization were 2.31 mm and 1.33 mm, respectively, which were close to the numerical results.

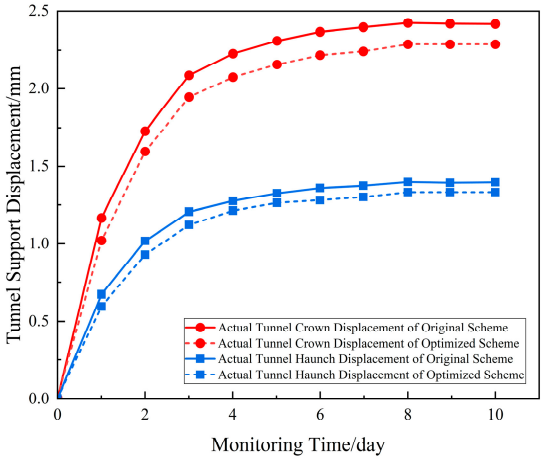


Figure 13. Comparison of crown and haunch displacements before and after optimization.

4. Discussion

4.1. Comparison with Previous Studies

This study investigated the surrogate-assisted optimization of S-RC hybrid support in fault fracture zone ground. As summarized in Table 6, previous studies have addressed efficient deformation prediction [25], vibration-oriented geometry and material optimization [8], interpretable support optimization [23], reliability-based support design [7], steel–concrete interface behavior [9], and segmental lining responses to fault movement [10]. The main contribution of the present study lies in the integrated application of OLHS, Kriging, SHAP, and NSGA-II to multi-component hybrid support under fault-zone conditions, with separate crown and haunch response predictions, parameter interpretation, and independent cost evaluation. Thickness dominated both SHAP rankings, consistent with stiffness-controlled rock–support interaction; in contrast, the differing width rankings suggest spatially different deformation responses. These interpretations remain specific to the surrogate model.

Table 6. Comparison of the scope of related studies and the present analysis.

Study	Reported Evidence/Contribution	Critical Comparison with the Present Study
Zheng et al. [25] (2023)	Compared surrogate accuracy and robustness for ground and structural deformation responses.	Provides an established benchmark for deformation surrogates; it does not directly optimize multi-component S-RC segment parameters against coupled deformation–cost objectives.
Liravi et al. [8] (2025)	Demonstrated surrogate-assisted exploration of tunnel design trade-offs for elastic-wave/vibration reduction.	Shows that surrogate-driven tunnel design is not new. Its dynamic vibration focus differs from fault-fracture-zone crown/haunch deformation and material-cost optimization.
Deng et al. [23] (2025)	Reported improvements for Grade III/IV surrounding rock and comparisons with field monitoring.	Closest methodological precedent: interpretability, multi-objective cost trade-offs, and field checks already exist. The present distinction is the S-RC hybrid support object and separate crown/haunch surrogate responses—not the tool combination itself.
Zhao et al. [22] (2026)	Connected settlement, settlement rate, and acceleration to support design under stability/cost constraints.	Offers more explicit hydro-mechanical and time-dependent treatment than the present deterministic model; the present case targets multi-component fault-zone hybrid segments instead.
Zhang et al. [7] (2024)	Integrated parameter uncertainty and failure-mode reliability into Pareto-based support design.	Establishes a stronger safety/uncertainty formulation. The present displacement–cost optimum cannot be regarded as reliability-verified or universally safe.

The scientific–theoretical significance of the study lies in demonstrating sample-efficient approximation of location-dependent lining responses through multi-objective optimization.

The workflow used 160 sampling analyses and direct verification, while approximately 160,000 candidate evaluations relied on surrogate predictions. This addresses the repeated-simulation burden within the investigated design space; however, the measured runtime remains unavailable.

The practical engineering significance lies in the reported reductions of 7.02%, 9.28%, and 12.84% in the crown displacement, haunch displacement, and material cost index, respectively. Direct numerical results and short-term field observations support the accuracy of the selected scheme under the project's conditions; however, its implementation requires practicable dimensions and material grades, together with project-specific structural safety checks.

4.2. Limitations

Although the present study demonstrates the feasibility of surrogate-assisted multi-objective optimization for hybrid segment support in fault fracture zones, several limitations remain.

First, the numerical model considers the mechanical behavior of the surrounding rock and support structure but does not account for groundwater pressure and seepage–stress coupling, which may affect tunnel deformation and structural stability; the spatial variability of surrounding rock properties, including local fractures and weak interlayers, was not characterized in detail, potentially affecting the accuracy of deformation predictions. Furthermore, the field monitoring period was limited to approximately 10 days, which is insufficient to fully evaluate the long-term deformation behavior of the tunnel.

Finally, the serrated joints between hybrid segments were simplified as an equivalent continuous structure, without explicitly considering local joint opening and sliding. In addition, the optimization framework was validated using only one tunnel case, and its applicability to different geological conditions and structural configurations requires further investigation.

4.3. Future Perspectives

Future research will focus on improving the accuracy, reliability, and applicability of the proposed optimization framework. First, more detailed geological investigations and coupled seepage–stress analyses will be incorporated to better represent the complex behavior of surrounding rock under different geological conditions. Second, explicit joint-contact models and longer-term field monitoring will be introduced to improve the evaluation and validation of hybrid segment performance. Finally, the proposed framework will be applied to different tunnel projects, while alternative surrogate models and optimization algorithms will be compared in terms of prediction accuracy, computational efficiency, and robustness. These improvements are expected to enhance the reliability and generalizability of the proposed method for practical tunnel support design.

5. Conclusions

This study investigated the deformation–cost optimization of S-RC hybrid segment support in a TBM tunnel crossing a fault fracture zone. Within the sampled design space, the Kriging models predicted crown and haunch displacements more accurately than the BP and RBF models. By predicting the two displacement responses separately and calculating the material-based support cost index directly, the framework enabled efficient evaluation of the competing objectives without repeated full numerical simulations. Its contribution lies in the integrated application of established methods rather than the development of a new optimization algorithm.

SHAP analysis showed that steel segment thickness was the most influential parameter for both displacement responses, while segment width had a greater influence on crown displacement. This difference suggests that changes in support parameters affect deformation differently around the tunnel lining. Therefore, considering crown and haunch displacements as separate objectives provides a more complete basis for support optimization.

The Pareto analysis showed that the three objectives could not reach their individual minima simultaneously. Compared with the reported original scheme, the compromise design selected by the normalized ideal-point method reduced crown displacement, haunch displacement, and the material-based support cost index by 7.02%, 9.28%, and 12.84%, respectively. Direct FLAC^{3D} calculations for the selected continuous design yielded displacements of 2.246 and 1.274 mm, differing from the Kriging predictions by only 0.18% and 0.31%. Short-term field observations of the practically adjusted scheme also showed lower displacements than the original scheme. These results support the selected design under the investigated conditions, although the field observations do not establish its long-term performance.

However, the present study still has some limitations. The numerical model represented serrated segment joints as an equivalent continuous structure and excluded groundwater effects, limiting the assessment of local joint behavior and hydro-mechanical responses. Field monitoring covered approximately 10 days in a single tunnel, and the cost index reflected material-based support cost rather than total construction cost. To address these limitations, future studies should first improve joint-contact and groundwater modeling to better represent the mechanical behavior of the support system. Structural safety constraints should then be incorporated to assess the feasibility of optimized designs. Finally, longer-term monitoring and additional tunnel cases would provide further evidence for evaluating the method under different engineering conditions.

Overall, this study provides an interpretable surrogate-assisted multi-objective optimization framework that combines displacement prediction, parameter sensitivity analysis, and deformation–cost evaluation for S-RC hybrid segment support. The framework may provide a useful reference for similar TBM tunnel projects.

Author Contributions: Conceptualization, G.Y. (Guofang Yang); methodology, G.Y. (Guofang Yang), D.L. and Q.G.; software, Q.G. and K.L.; validation, D.L. and G.Y. (Guanfei Yang); formal analysis, G.Y. (Guofang Yang), G.Y. (Guanfei Yang) and K.L.; writing—original draft, G.Y. (Guofang Yang); writing—review and editing, G.Y. (Guofang Yang) and B.W.; funding acquisition, B.W. All authors have read and agreed to the published version of the manuscript.

Funding: This work is supported by the National Natural Science Foundation of China (51908440), the Natural Science Foundation of Shaanxi province, China (2021JM-426), and the Key Science and Technology R&D Project of CCCC-SHB Co., Ltd., China (2024S-3-8).

Institutional Review Board Statement: Not applicable.

Informed Consent Statement: Not applicable.

Data Availability Statement: The original contributions presented in this study are included in the article. Further inquiries can be directed to the corresponding author.

Acknowledgments: We sincerely thank the anonymous reviewers for their insightful and constructive comments, which helped improve the quality of this manuscript.

Conflicts of Interest: The authors declare that they have no known competing financial interests or personal relationships that could have appeared to influence the work reported in this paper. Guofang Yang, Dongming Liu, Qiang Guo, and Guanfei Yang are employees of the company CCCC-SHB Fourth Engineering Co., Ltd., Luoyang, China, who provided funding and technical support for the work.

References

1. Wang, M.S. Tunneling by TBM shield in China: State-of-art, Problems and Proposals. *Tunn. Constr.* **2014**, *34*, 179–187. (In Chinese)
2. Li, Q.L.; Li, Y.Z.; Pei, C.Y. Study on the effect of surface pre-grouting reinforcement for TBM tunnel in gully fault fracture zones. *China Civ. Eng. J.* **2024**, *57*, 52–58. (In Chinese)
3. Li, H.; Wang, L.B.; Wang, F.Q.; Li, Z. Research on multi-objective optimization of support parameters of high-speed railway tunnel. *J. For. Eng.* **2021**, *6*, 169–175. (In Chinese)
4. Qu, Z.M.; Xue, Y.G.; Kong, F.M.; Zhou, C.; Qu, J.; Liu, Z. Research on deformation mechanism and support structure optimization of composite strata in red beds tunnel excavation. *Tunn. Undergr. Space Technol.* **2026**, *168*, 107132. [CrossRef]
5. Cui, J.Q.; Wu, S.C.; Cheng, H.Y.; Kui, G.; Zhang, H.; Hu, M.; He, P. Composite interpretability optimization ensemble learning inversion surrounding rock mechanical parameters and support optimization in soft rock tunnels. *Comput. Geotech.* **2024**, *165*, 105877. [CrossRef]
6. Yu, Y.X.; Ma, T.Y.; Tang, L.Y.; Li, W.; Ma, Y.J.; Jia, S.B. Inversion Analysis and Application of the Deformation Law of Anchored Surrounding Rock in Deep-Buried Tunnels under Stress-Displacement-Seepage Coupling. *Railw. Stand. Des.* **2026**, *70*, 1–11. (In Chinese)
7. Zhang, Z.; Li, S.; Zhang, Y.; Zhou, Y.; Ji, J. Multi-objective reliability-based robust design for a rock tunnel support system using Pareto optimality. *Int. J. Numer. Anal. Methods Geomech.* **2024**, *48*, 3350–3368. [CrossRef]
8. Liravi, H.; Bui, H.G.; Kaewunruen, S.; Colaço, A.; Ninić, J. Bayesian optimization of underground railway tunnels using a surrogate model. *Data-Centric Eng.* **2025**, *6*, e32. [CrossRef]
9. Zhang, J.L.; Liu, X.; Ren, T.Y.; Shi, Y.-M.; Yuan, Y. Numerical analysis of tunnel segments strengthened by steel–concrete composites. *Undergr. Space* **2022**, *7*, 1115–1124. [CrossRef]
10. Ramesh, A.; Rashiddel, A.; Hajihassani, M.; Dias, D.; Kiani, M. Interaction of segmental tunnel linings and dip-slip faults—Tabriz subway tunnels. *Appl. Sci.* **2023**, *13*, 7866. [CrossRef]
11. Chang, X.; Sun, J.; Guo, L. Mechanical performances of concrete-filled steel pipe composite segments in complex geological conditions. *Buildings* **2024**, *14*, 2961. [CrossRef]
12. Neu, G.E.; Edler, P.; Freitag, S.; Gudžulić, V.; Meschke, G. Reliability based optimization of steel-fibre segmental tunnel linings subjected to thrust jack loadings. *Eng. Struct.* **2022**, *254*, 113752. [CrossRef]
13. Bao, X.; Li, Y.; Zhang, X.; Wu, X.; Chen, X.; Cui, H. Mechanical behaviors of hybrid fiber-rebar reinforced concrete lining under ground surcharge loads—3D numerical simulation combined with full-scale test. *Eng. Struct.* **2025**, *334*, 120257. [CrossRef]
14. Zhang, F.; De Corte, W.; Taerwe, L.; Cao, W.; Liu, X. A study on the bending stiffness of reinforced concrete tunnel segments with added steel fibers. *Materials* **2025**, *18*, 48. [CrossRef] [PubMed]
15. Sun, Y.; Yu, Y.; Wang, J.; Wang, L. Interface failure of segmental tunnel lining strengthened with steel plates based on fracture mechanics. *Front. Struct. Civ. Eng.* **2024**, *18*, 137–149. [CrossRef]
16. Spagnuolo, S.; Meda, A. Precast CSA-based concrete tunnel lining segments reinforced with GFRP bars: Challenges and opportunities. *Constr. Build. Mater.* **2024**, *425*, 136007. [CrossRef]
17. Zheng, Q.; Zhang, X.; Shen, Y.S.; Qiu, J.-T.; Wang, Y.-D.; Chen, K.-F. Failure mechanism of segmental lining structure in fault-crossing tunnel: An experimental and numerical investigation. *J. Cent. South Univ.* **2023**, *30*, 2392–2410. [CrossRef]
18. Wang, S.; Ding, Z.; Shi, C.; Cai, H.; Chen, Y.; Ding, W.; Huang, J. Dislocation response of ECC-RC composite supporting structures of tunnels passing through active fault. *Sci. Rep.* **2024**, *14*, 15199. [CrossRef] [PubMed]
19. Xu, W.T.; Wu, H.G.; Shi, C.Z.; Xia, Y.; Yang, X.-Y. Design and optimization of an innovative lining structure for high-pressure water transmission tunnels subjected to strike-slip fault creep. *Sci. Rep.* **2025**, *15*, 10655. [CrossRef] [PubMed]
20. Hu, H.; Lan, Y.; Liu, Y.; Qiu, W. Experimental study on the damage performance and forced response of concrete lining in fault-crossing tunnel. *Sci. Rep.* **2024**, *14*, 2120. [CrossRef] [PubMed]
21. Zhao, X.; Han, K.; Ju, J.W.; Chen, X.; Chen, W.; Xiong, H. Numerical analysis of size effect on the deformation behavior and damage evolution mechanism of segmental tunnel lining rings. *Int. J. Damage Mech.* **2023**, *32*, 600–622. [CrossRef]
22. Zhao, Y.; Li, Y.L.; She, L.; Hu, C.-C.; Li, B.; Wang, T.; Sun, X.-J.; Li, X.-J. Physics-data driven approach for multi-objective intelligent prediction and optimization of deep soft rock tunnel stability. *Transp. Geotech.* **2026**, *60*, 102014. [CrossRef]
23. Deng, Z.A.; Zhang, J.X.; Zhang, Y.X.; Sun, Y. Multi—Objective optimization method for tunnel support schemes driven by surrogate models. *J. Hydroelectr. Eng.* **2025**, *44*, 59–71. (In Chinese)
24. Kim, D.; Kwon, K.; Pham, K.; Oh, J.-Y.; Choi, H. Surface settlement prediction for urban tunneling using machine learning algorithms with Bayesian optimization. *Autom. Constr.* **2022**, *140*, 104331. [CrossRef]
25. Zheng, H.; Mooney, M.; Gutierrez, M. Surrogate model for 3D ground and structural deformations in tunneling by the sequential excavation method. *Comput. Geotech.* **2023**, *154*, 105142. [CrossRef]
26. Gottardi, N.; Freitag, S.; Meschke, G. Real-time estimation of the structural utilization level of segmental tunnel lining. *Undergr. Space* **2024**, *17*, 132–145. [CrossRef]

27. Tian, Z.; Zhou, S.; Lee, A.W.L.; Shan, Y.; Detmann, B. How to identify earth pressures on in-service tunnel linings: Insights from Bayesian inversion to address non-uniqueness. *Transp. Geotech.* **2024**, *48*, 101344. [CrossRef]
28. Liu, W.L.; Chen, Y.; Liu, T.X.; Li, J.; Chen, Y. Shield tunneling efficiency and stability enhancement based on interpretable machine learning and multi-objective optimization. *Undergr. Space* **2025**, *22*, 320–336. [CrossRef]
29. Tao, Y.Q.; He, W.; Sun, H.L.; Cai, Y.; Chen, J. Multi-objective optimization-based prediction of excavation-induced tunnel displacement. *Undergr. Space* **2022**, *7*, 735–747. [CrossRef]
30. Bui, H.G.; Cao, B.T.; Freitag, S.; Hackl, K.; Meschke, G. Surrogate modeling for interactive tunnel track design using the cut finite element method. *Eng. Comput.* **2023**, *39*, 4025–4043. [CrossRef]
31. Zendaki, Y.; Cao, B.T.; Alsahly, A.; Freitag, S.; Meschke, G. A simulation-based software to support the real-time operational parameters selection of tunnel boring machines. *Undergr. Space* **2024**, *14*, 176–196. [CrossRef]
32. Liu, H.; Su, H.; Sun, L.; Dias-Da-Costa, D. State-of-the-art review on the use of AI-enhanced computational mechanics in geotechnical engineering. *Artif. Intell. Rev.* **2024**, *57*, 196. [CrossRef]
33. Sheil, B.; Anagnostopoulos, C.; Buckley, R.; Ciantia, M.O.; Febrianto, E.; Fu, J.; Gao, Z.; Geng, X.; Gong, B.; Hanley, K.; et al. Artificial intelligence transformations in geotechnics: Progress, challenges and future enablers. *Comput. Geotech.* **2026**, *189*, 107604. [CrossRef]
34. Sioutas, K.N.; Benardos, A. Boosting model interpretability for transparent ML in TBM tunneling. *Appl. Sci.* **2024**, *14*, 11394. [CrossRef]
35. Sacks, J.; Welch, W.J.; Mitchell, T.J.; Wynn, H.P. Design and analysis of computer experiments. *Stat. Sci.* **1989**, *4*, 409–423. [CrossRef]
36. Morris, M.D.; Mitchell, T.J. Exploratory designs for computational experiments. *J. Stat. Plan. Inference* **1995**, *43*, 381–402. [CrossRef]
37. Deb, K.; Pratap, A.; Agarwal, S.; Meyarivan, T. A fast and elitist multiobjective genetic algorithm: NSGA-II. *IEEE Trans. Evol. Comput.* **2002**, *6*, 182–197. [CrossRef]
38. Lundberg, S.M.; Erion, G.; Chen, H.; DeGrave, A.; Prutkin, J.M.; Nair, B.; Katz, R.; Himmelfarb, J.; Bansal, N.; Lee, S.-I. From local explanations to global understanding with explainable AI for trees. *Nat. Mach. Intell.* **2020**, *2*, 56–67. [CrossRef] [PubMed]
39. *GB 50017-2017*; Standard for Design of Steel Structures. China Architecture & Building Press: Beijing, China, 2017. (In Chinese)
40. *GB 50164-2011*; Standard for Quality Control of Concrete. China Architecture & Building Press: Beijing, China, 2011. (In Chinese)
41. Liu, X.B.; Wang, Y.; Wang, W.Q.; He, S.H.; Ma, J.F. Study on Key Excavation Parameters of Shallow Super-large-span Four-track Tunnel Under Grade-V Surrounding Rock mass. *Railw. Stand. Des.* **2024**, *68*, 132–140.
42. Tao, Y.Q.; Sun, H.L.; Cai, Y.Q. Bayesian back analysis considering constraints. *Chin. J. Geotech. Eng.* **2021**, *43*, 1878–1886.
43. Zeng, T.M.; Wang, J.F.; Wu, X.G.; Tian, J.K.; Tao, W.T.; Yang, S.; Chen, B. Multi-objective optimization of displacement of shield tunneling underpass existing tunnel based on GA-LSSVM combining NSGA-II. *Railw. Stand. Des.* **2022**, *66*, 98–104. (In Chinese)

Disclaimer/Publisher's Note: The statements, opinions and data contained in all publications are solely those of the individual author(s) and contributor(s) and not of MDPI and/or the editor(s). MDPI and/or the editor(s) disclaim responsibility for any injury to people or property resulting from any ideas, methods, instructions or products referred to in the content.